Micron-scale graphene transport simulation using scaled graphene

Ming-Hao Liu (劉明豪),[1,*] Peter Rickhaus,[2] Péter Makk,[2] Endre Tóvári,[3] Romain Maurand,[4] Fedor Tkatschenko,[1] Markus Weiss,[2] Christian Schönenberger,[2] and Klaus Richter[1]

[1]*Institut für Theoretische Physik, Universität Regensburg, D-93040 Regensburg, Germany*
[2]*Department of Physics, University of Basel, Klingelbergstrasse 82, CH-4056 Basel, Switzerland*
[3]*Department of Physics, Budapest University of Technology and Economics and Condensed Matter Research Group of the Hungarian Academy of Sciences, Budafoki ut 8, 1111 Budapest, Hungary*
[4]*University Grenoble Alpes, CEA-INAC-SPSMS, F-38000 Grenoble, France*

(Dated: April 10, 2017)

Artificial graphene consisting of honeycomb lattices other than the atomic layer of carbon have been shown to exhibit electronic properties similar to real graphene. Here, we show in the opposite logic that transport properties of real graphene can be captured by simulations using "theoretical artificial graphene". We derive a simple condition, along with its restrictions, to achieve band structure invariance for a scalable graphene lattice. Using the properly scaled artificial graphene, we perform quantum transport calculations within single-particle tight-binding models to simulate high-quality suspended graphene *pn* junction devices. Good agreement between experiment and theory, for both zero-field- and magneto-transport, proves that the physics of real graphene can indeed be captured by studying the scaled graphene. Our findings indicate that transport simulations for graphene can be done with a much smaller number of atomic sites, paving the way to fully two-dimensional micron-scale graphene device simulations.

PACS numbers: 72.80.Vp, 72.10.-d, 73.23.Ad

Graphene is a promising material for its special electrical, optical, thermal, and mechanical properties. In particular, the conic electronic structure that mimics two-dimensional (2D) massless Dirac fermions attracts much attention on both the academic and industrial side. Soon after the "debut" of single layer graphene [1, 2] and the subsequent confirmation of its relativistic nature [3, 4], the exploration of Dirac fermions in condensed matter has been further extended to honeycomb lattices other than graphene, including optical lattices [5–7], semiconductor nanopatterning [8–11], molecular arrays on Cu(111) surface [12], or even macroscopic systems of dielectric resonators for microwave propagation [13, 14], all of which have been shown to exhibit similar electronic properties as real graphene and hence are referred to as artificial graphene [15].

Here, we show in the opposite logic that transport properties of real graphene can be captured by simulations using "theoretical artificial graphene", by which we mean a honeycomb lattice with its lattice spacing a different from the carbon-carbon bond length a_0 of real graphene; see Fig. 1. From a theoretical point of view, this can be achieved only if the considered theoretical artificial lattice, which will be shortly referred to as artifical graphene or scaled graphene, has its energy band structure identical to that of real graphene. In this paper, we first derive a simple condition, along with its restrictions, to achieve the band structure invariance of graphene with its bond length scaled from a_0 to a, even in the presence of magnetic field. We then present realistic conductance simulations for a two-terminal suspended graphene device, using a properly scaled graphene. Good agreement between theory and experiment proves that the physics of real graphene can indeed be captured by studying artificial graphene. Notably, the feature of the measured conductance at zero magnetic field can be well reproduced by our simulation even using a scaling factor of one hundred.

We begin our discussion with the standard tight-binding model for 2D graphite [16], i.e., bulk graphene, and focus on the low-energy range ($|E| \lesssim 1\,\mathrm{eV}$) which is usually addressed in transport measurements for graphene. In this regime, the effective Dirac Hamiltonian $H_{\mathrm{eff}} = v_F \vec{\sigma}\cdot\mathbf{p}$ associated with the celebrated linear band structure $E(\mathbf{k}) = \pm\hbar v_F|\mathbf{k}|$ describes the graphene system well. Here $v_F \approx 10^8\,\mathrm{cm\,s^{-1}}$ is the Fermi velocity in graphene, and $\hbar\mathbf{k}$, the eigenvalue of the operator $\vec{\sigma}\cdot\mathbf{p}$ [Pauli matrices $\vec{\sigma} = (\sigma_x, \sigma_y)$ act on the pseudospin properties], is the quasimomentum with $\mathbf{k}$ defined

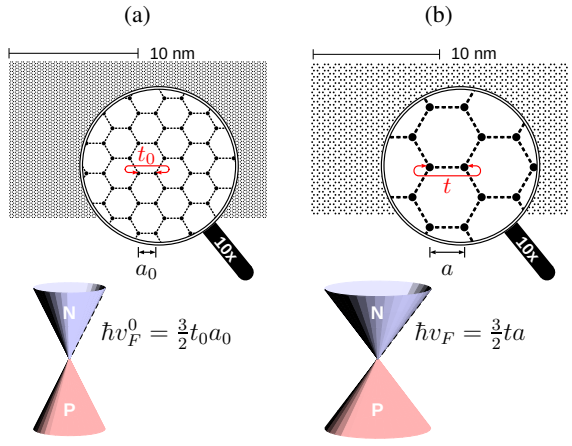

FIG. 1. (Color online) Schematic of a sheet of (a) real graphene and (b) scaled graphene and their conical low-energy band structures. In (a), the lattice spacing $a_0 \approx 0.142\,\mathrm{nm}$, the hopping energy $t_0 \approx 2.8\,\mathrm{eV}$, and the Fermi velocity $v_F^0 \approx 10^8\,\mathrm{cm\,s^{-1}}$.

relative to the K or K' point in the first Brillouin zone. In terms of the tight-binding parameters, one replaces $\hbar v_F$ with $(3/2)t_0a_0$, where $t_0 \approx 2.8\,\mathrm{eV}$ is the nearest neighbor hopping parameter and $a_0 \approx 0.142\,\mathrm{nm}$ is the lattice site spacing, i.e., $E_0(k) = (3/2)t_0a_0k$ for real graphene [17]. Now, we consider the scaled graphene described by the same tight-binding model but with hopping parameter t and lattice spacing a, and introduce a scaling factor s_f such that $a = s_f a_0$. The real and scaled graphene sheets along with their low-energy band structures are schematically sketched in Fig. 1. The low-energy dispersion for scaled graphene is naturally expected to be $E(k) = (3/2)tak$. Thus to keep the energy band structure unchanged while scaling up the bond length by a factor of s_f, the condition

$$a = s_f a_0, \qquad t = \frac{t_0}{s_f}. \tag{1}$$

becomes evident.

Clearly, Eq. (1) applies only when the linear approximation is valid. In terms of the long wavelength limit, this means that the Fermi wavelength should be much longer than the lattice spacing: $\lambda_F \gg a$, from which using Eq. (1) one can deduce the validity criterion

$$s_f \ll \frac{3t_0\pi}{|E_{\max}|}, \tag{2}$$

where $E_{\max}$ is the maximal energy of interest for investigating a particular real graphene system. Considering graphene on typical Si/300nm SiO_2 substrate, the usually accessed carrier density range is less than $10^{13}\,\mathrm{cm}^{-2}$ [1]. This implies that the energy range of interest lies within $|E_{\max}| \lesssim 0.4\,\mathrm{eV}$, leading to $s_f \ll 66$ from Eq. (2) (using $t_0 = 2.8\,\mathrm{eV}$). For suspended graphene, typical carrier densities can hardly reach $10^{12}\,\mathrm{cm}^{-2}$ [18], so that $|E_{\max}| \lesssim 0.1\,\mathrm{eV}$ allows for a larger range of the scaling factor, $s_f \ll 264$.

In the presence of an external magnetic field, the Peierls substitution [19] is the standard method to take into account the effect of a uniform out-of-plane magnetic field B_z within the tight-binding formulation. In addition to the long wavelength limit (2), the validity of the Peierls substitution, however, imposes a further restriction for the scaling [20]: $l_B \gg a$, where $l_B = \sqrt{\hbar/eB_z}$ is the magnetic length. In terms of $a = s_f a_0$ given in Eq. (1), this restriction reads

$$s_f \ll \frac{l_B}{a_0} \approx \frac{180}{\sqrt{B_z}}, \tag{3}$$

where B_z is in units of T. Equations (1)–(3) complete the description of band structure invariance for scaled graphene.

The above discussion is based on bulk graphene, but the listed conditions apply equally well to finite-width graphene ribbons. To show a concrete example of band structure invariance under scaling, we consider a 200-nm-wide armchair ribbon and compare the band structures of the genuine case with $s_f = 1$ and the scaled case with $s_f = 4$, as shown in Fig. 2(a). Within the relatively large energy range of $|E| \leq 0.5\,\mathrm{eV}$, the

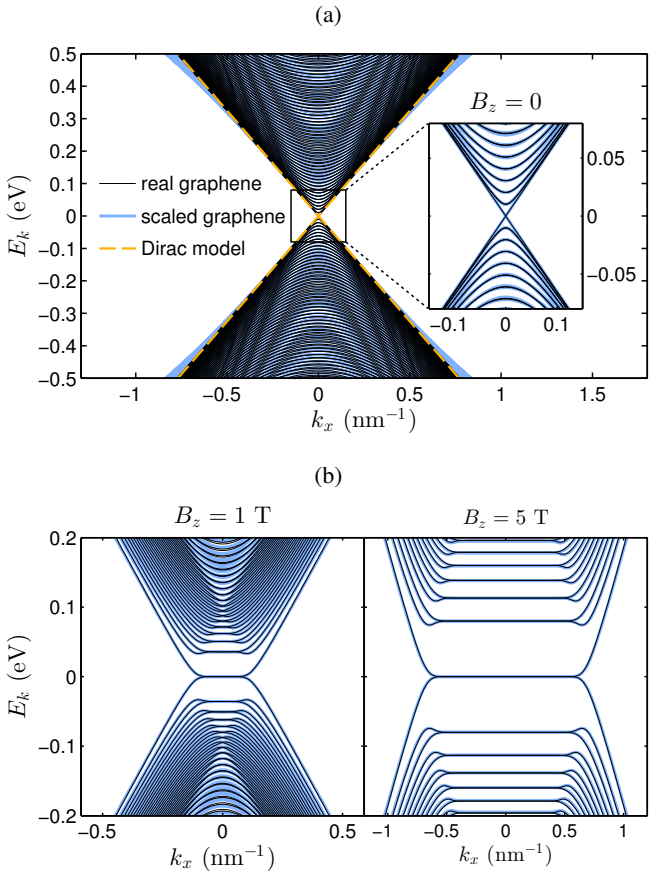

FIG. 2. (Color online) Band structure consistency check using an armchair graphene ribbon with width 200 nm, (a) in the absence of magnetic field, and (b) in the presence of a uniform magnetic field $B_z = 1\,\mathrm{T}$ (left) and $B_z = 5\,\mathrm{T}$ (right). Inset in (a) shows the zoom-in plot for the boxed region of the main panel. The comparison is done for both (a) and (b) between the real graphene with $s_f = 1$ and scaled graphene with $s_f = 4$, which correspond to chain numbers $N_a = 800$ and $N_a = 200$, respectively.

genuine graphene band structure is well bound by the linear Dirac model that corresponds to the ideal bulk graphene. On the other hand, the scaled graphene band structure starts to exhibit a nonlinear cone shape at about $|E| \gtrsim 0.2\,\mathrm{eV}$, where the long wavelength limit (2) no longer holds. In the low energy range [inset of Fig. 2(a)], one observes a nearly perfect consistency between the genuine and scaled graphene band structures. The model remains consistent when a magnetic field is applied, as seen in Fig. 2(b), where we consider $B_z = 1\,\mathrm{T}$ and 5 T, both of which still lie within the restriction (3) for the present $s_f = 4$ example. The band structure invariance based on Eqs. (1)–(3) can be easily shown to hold also for zigzag graphene ribbons.

Having demonstrated that under proper conditions (1)–(3) the scaled graphene band structure can be identical to that of real graphene, we next perform full quantum transport simulations using scaled graphene, taking into account the three-dimensional geometry of a real experimental graphene de-

vice. To this end, we have fabricated ultra-clean suspended graphene *pn* junctions. First, bottom gates were prepatterned on a Si wafer with 300 nm SiO_2 oxide. Afterwards, the wafer was spin-coated with lift-off resist (LOR), and the graphene was transferred on top following the method described in Ref. 21. Palladium contacts to graphene were made by e-beam lithography and thermal evaporation, and the device was suspended, by exposing and developing the LOR resist. Finally, the graphene was cleaned by current annealing at 4 K. The fabrication method is described in Refs. 22 and 23 in detail.

Following the device design of our experiment [sketched in Fig. 3(a) with actual dimensions adopted in the simulation], we first build the three-dimensional (3D) electrostatic model to obtain the self-partial capacitances [24] of the individual metal contacts and bottom gates, which are computed by the finite-element simulator FEniCS [25] combined with the mesh generator GMSH [26]. The extracted self-partial capacitances from the electrostatic simulation provide us the realistic carrier density profile [27] $n(x,y)$ at any combination of the left and right bottom gate voltages, V_{bogL} and V_{bogR}, respectively. In the inset of Fig. 3(a), we plot the mean carrier density $\bar{n}$ averaged over the whole suspended graphene region as a function of $V_{\mathrm{bog}} = V_{\mathrm{bogL}} = V_{\mathrm{bogR}}$. The slope reveals a charging efficiency of the connected bottom gates of about $10^{10}\,\mathrm{cm}^{-2}\,\mathrm{V}^{-1}$, which will be later compared with the experimental value extracted from the unipolar quantum Hall data.

In the absence of magnetic field, the Fermi energy as a function of carrier density within the low-energy range can be well described by the Dirac model, $E(n) = \mathrm{sgn}(n)\hbar v_F\sqrt{\pi|n|}$. This suggests: for a given carrier density at (x,y), applying a local energy band offset defined by $V(x,y) = -\,\mathrm{sgn}[n(x,y)]\hbar v_F\sqrt{\pi|n(x,y)|}$ guarantees that the locally filled highest level fulfills the amount of the simulated carrier density $n(x,y)$ and is globally fixed at $E = 0$ for all (x,y). We therefore consider the model Hamiltonian,

$$H_{\mathrm{model}} = \sum_i V(x_i,y_i)c_i^\dagger c_i - t(s_f)\sum_{\langle i,j\rangle} c_i^\dagger c_j, \qquad (4)$$

and apply the Landauer-Büttiker formalism [28] to calculate the transmission function T at energy $E = 0$ and zero temperature. In Eq. (4), the indices i and j run over the lattice sites within the scattering region defined by an artificial graphene scaled by s_f, and the second term contains the nearest neighbor hopping elements with strength $t(s_f)$ given in Eq. (1).

For zero-field transport, we compute the conductance map $G(V_{\mathrm{bogR}}, V_{\mathrm{bogL}})$ from the transmission function T using $G = (e^2/h)[T^{-1} + R_c/(h/e^2)]^{-1}$, where the contact resistance is deduced from the quantum Hall measurement to be $R_c \approx 1080\,\Omega \approx 4.2\times10^{-2}(h/e^2)$. The measured and simulated conductance maps in the absence of magnetic field are compared in Fig. 3(b). Both exhibit pronounced Fabry-Pérot interference patterns in the bipolar blocks similar to previously reported ballistic graphene *pn* junctions [29, 30]. Strikingly, the theory data reported in Fig. 3(b) is based on a scaled graphene with $s_f = 100$, and the result agrees qualitatively well with the experiment. The present device allows for such a huge

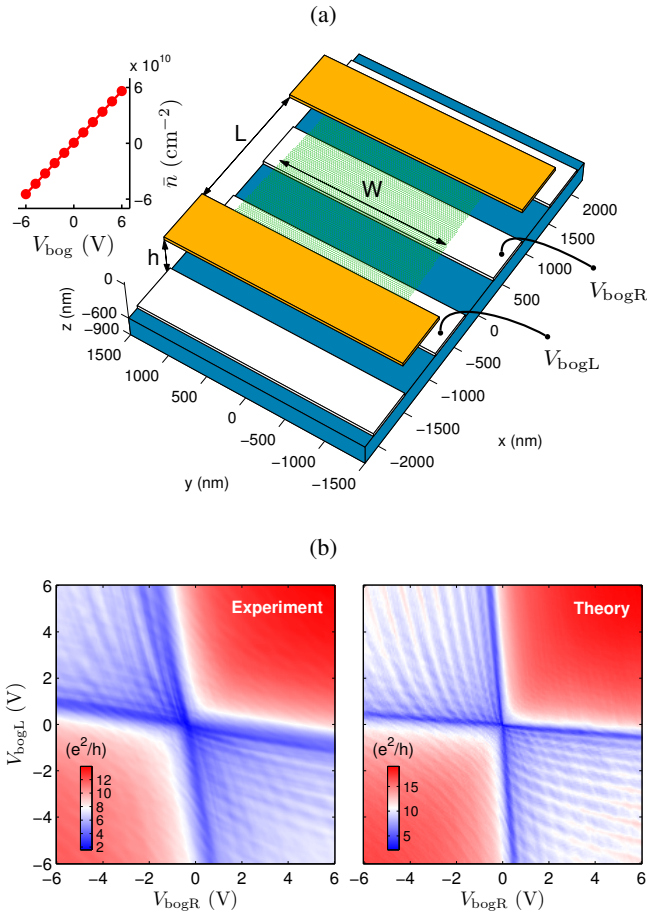

FIG. 3. (Color online) (a) Device sketch of the suspended graphene for electrostatic modeling and transport simulation, following the experiment design with suspension height $h = 600$ nm, contact spacing $L = 1680$ nm, and average flake width $W = 2125$ nm. Inset: Mean carrier density as a function of the voltage on the two bottom gates when they are connected to each other, $V_{\mathrm{bogL}} = V_{\mathrm{bogR}} = V_{\mathrm{bog}}$, based on a 3D electrostatic simulation. (b) Experimental and theoretical data of the two-terminal conductance. The former was measured at low temperature $T = 1.4$ K, while the latter was calculated by using an ideal $s_f = 100$ scaled clean graphene at zero temperature.

scaling factor due to the very low energy. From the estimated maximal carrier density [inset of Fig. 3(a)], we find $|E_{\mathrm{max}}| \approx 28$ meV, such that Eq. (2) roughly gives $s_f \ll 10^3$, suggesting that $s_f = 100$ is acceptable. Simulations with smaller s_f have been performed and do not significantly differ from the reported map.

Similar to the zero-field case, the first step for an accurate transport simulation at finite B_z is to extract the proper energy band offset from the given carrier density through the carrier-energy relation, for which an exact analytical formula does not exist. Numerically, the carrier density as a function of energy and magnetic field, $n(E,B_z)$, can be computed also using the Green's function method [27]. Once $n(E,B_z)$ is obtained, one can deduce $E(n,B_z)$ by interpolation, and the desired energy band offset is again given by the negative of it.

Thus the magnetic field in the transport simulation requires, in addition to the Peierls substitution of the hopping parameter, the modification on the on-site energy term of Eq. (4), $V(x_i,y_i) \to V(x_i,y_i;B_z) = -E(n(x_i,y_i),B_z)$, where $n(x_i,y_i)$ is obtained from the same electrostatic simulation and is assumed to be unaffected by the magnetic field, i.e., we assume the electrostatic charging ability of the bottom gates is not influenced by the magnetic field.

Figure 4(a) shows the measured unipolar conductance map $G(B_z,V_{\rm bog})$ with the two bottom gates connected together. The pronounced fan diagram allows for a precise evaluation of the gate efficiency and chemical doping concentration [27], which are found to be $1.24\times10^{10}\,{\rm cm}^{-2}\,{\rm V}^{-1}$ and $-3.72\times10^{9}\,{\rm cm}^{-2}$, respectively. By subtracting the contact resistance $R_c \approx 1080\,\Omega$, the quantized conductance at low field up to 0.2 T is compared with the computed transmission function using $s_f = 50$ scaled graphene in Fig. 4(b), where the color range is adjusted to highlight the conductance plateaus up to $\nu = \pm 14$.

Despite the rather consistent Landau fan diagrams in both experiment and theory maps of Fig. 4(b), a closer look shows the slightly different gate efficiencies (slope of the fan lines) as already noted above. In addition, the minimal B_z required to quantize the conductance in the experiment is larger than that in the simulation possibly because of thermal fluctuations not considered in the calculations. Note that here we have considered Anderson-type disorder by adding to the model Hamiltonian (4) the potential term $\sum_i U_i c_i^\dagger c_i$, where U_i is a random number $U_i \in [-U_{\rm dis}/2, U_{\rm dis}/2]$ with disorder strength $U_{\rm dis} = 3\,{\rm meV}$ used in the theory map of Fig. 4(b). The quantized conductance in the simulation is found to be robust against the disorder potential, whose quantitative effect is yet to be established for the scaled graphene and is beyond the scope of the present discussion.

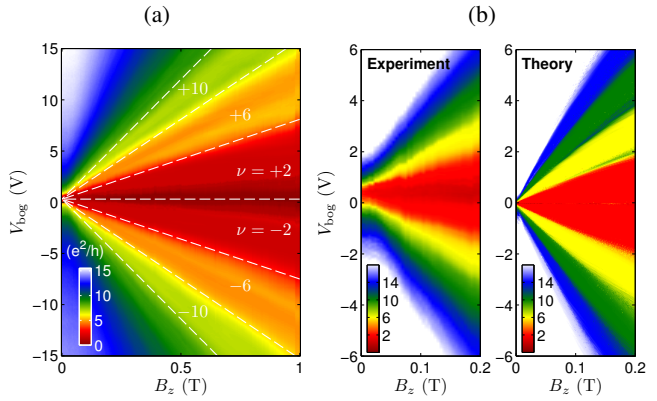

FIG. 4. (Color online) (a) Experimental data of the conductance measured with the two bottom gates connected to each other ($V_{\rm bogL} = V_{\rm bogR} = V_{\rm bog}$) and magnetic field B_z sweep up to 1 T. The lowest 6 quantized conductance plateaus labeled by filling factor $\nu = \pm2, \pm6, \pm10$ are separated by the fitting fan lines [27]. (b) By subtracting the deduced contact resistance $R_c \approx 1080\,\Omega$, the experimental data at low field is compared with the theory data of the computed transmission function.

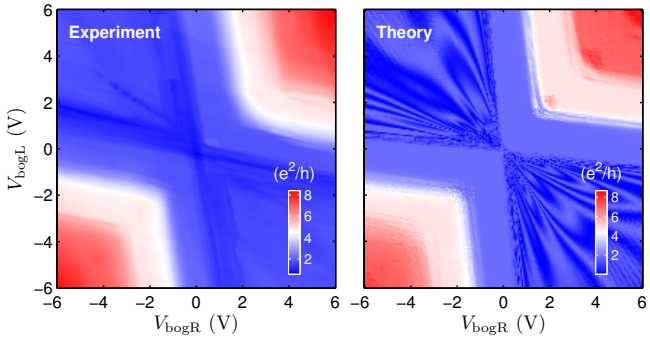

FIG. 5. (Color online) Conductance $G(V_{\rm bogR},V_{\rm bogL})$ measured (left) and simulated (right) at $B_z = 0.2\,{\rm T}$. The simulation is based on $s_f = 50$ artificial graphene in the presence of Anderson-type disorder with fluctuation strength $U_{\rm dis} = 6\,{\rm meV}$.

Finally, we compare the conductance maps $G(V_{\rm bogR},V_{\rm bogL})$ measured and simulated at $B_z = 0.2\,{\rm T}$ in Fig. 5, using $s_f = 50$ scaled graphene in the presence of disorder potential with $U_{\rm dis} = 6\,{\rm meV}$. We observe very good agreement in the conductance range as well as in the conductance features in the unipolar blocks. In the bipolar blocks, however, the simulation reveals a fine structure that is found to be sensitive to disorder potential and the edge disorder, but is not observed in the present experimental data. Nevertheless, the conductance in the bipolar blocks varies between 0 and $2e^2/h$ in both experiment and theory, and neither of them exhibits the fractional plateaus [31]. Thus the bipolar blocks of Fig. 5 reveal a conductance behavior due to the ballistic smooth graphene *pn* junctions very different from the diffusive sharp ones [32–34].

In conclusion, we have shown that the physics of real graphene can be well captured by studying properly scaled, artificial graphene. This important fact indicates that for low-energy transport simulations in graphene based on tight-binding models, the required number of lattice sites need not be as massive as in actual graphene sheets. The introduced parameter s_f scales down the amount of the Hamiltonian matrix elements of the simulated graphene flake by a factor of s_f^{-4}, and hence strongly reduces the memory demand [27]; the scaling applies also to bilayer graphene [27]. Our findings advance the power of quantum transport simulations for graphene in a simpler and more natural way as compared to the finite difference method for massless Dirac fermions [35], paving the way to fully 2D micron-scale graphene device simulations.

We thank J. Bundesmann, S. Essert, and V. Krueckl and J. Michl for valuable suggestions. Financial support by the Deutsche Forschungsgemeinschaft within programs GRK 1570 and SFB 689, by the Hans Böckler Foundation, by the Swiss NSF, the EU FP7 project SE2ND, the ERC Advanced Investigator Grant QUEST, the ERC 258789, the Swiss NCCR Nano QSIT, and Graphene Flagship is gratefully acknowledged.

* minghao.liu.taiwan@gmail.com

[1] K. S. Novoselov, A. K. Geim, S. V. Morozov, D. Jiang, Y. Zhang, S. V. Dubonos, I. V. Grigorieva, and A. A. Firsov, Science **306**, 666 (2004).

[2] C. Berger, Z. Song, T. Li, X. Li, A. Y. Ogbazghi, R. Feng, Z. Dai, A. N. Marchenkov, E. H. Conrad, P. N. First, and W. A. de Heer, The Journal of Physical Chemistry B **108**, 19912 (2004).

[3] Y. Zhang, Y.-W. Tan, H. L. Stormer, and P. Kim, Nature **438**, 201 (2005).

[4] K. S. Novoselov, A. K. Geim, S. V. Morozov, D. Jiang, M. I. Katsnelson, I. V. Grigorieva, S. V. Dubonos, and A. A. Firsov, Nature **438**, 197 (2005).

[5] S.-L. Zhu, B. Wang, and L.-M. Duan, Phys. Rev. Lett. **98**, 260402 (2007).

[6] B. Wunsch, F. Guinea, and F. Sols, New Journal of Physics **10**, 103027 (2008).

[7] T. Uehlinger, G. Jotzu, M. Messer, D. Greif, W. Hofstetter, U. Bissbort, and T. Esslinger, Phys. Rev. Lett. **111**, 185307 (2013).

[8] C.-H. Park and S. G. Louie, Nano Letters **9**, 1793 (2009), http://pubs.acs.org/doi/pdf/10.1021/nl803706c.

[9] M. Gibertini, A. Singha, V. Pellegrini, M. Polini, G. Vignale, A. Pinczuk, L. N. Pfeiffer, and K. W. West, Phys. Rev. B **79**, 241406 (2009).

[10] E. Räsänen, C. A. Rozzi, S. Pittalis, and G. Vignale, Phys. Rev. Lett. **108**, 246803 (2012).

[11] E. Kalesaki, C. Delerue, C. Morais Smith, W. Beugeling, G. Allan, and D. Vanmaekelbergh, Phys. Rev. X **4**, 011010 (2014).

[12] K. K. Gomes, W. Mar, W. Ko, F. Guinea, and H. C. Manoharan, Nature **483**, 306 (2012).

[13] U. Kuhl, S. Barkhofen, T. Tudorovskiy, H.-J. Stöckmann, T. Hossain, L. de Forges de Parny, and F. Mortessagne, Phys. Rev. B **82**, 094308 (2010).

[14] M. Bellec, U. Kuhl, G. Montambaux, and F. Mortessagne, Phys. Rev. B **88**, 115437 (2013).

[15] M. Polini, F. Guinea, M. Lewenstein, H. C. Manoharan, and V. Pellegrini, Nature Nanotechnology **8**, 625 (2013).

[16] P. R. Wallace, Phys. Rev. **71**, 622 (1947).

[17] Note that the next nearest neighbor hopping t' does not play a role for describing the low-energy physics of graphene, and will not be considered in this work.

[18] K. Bolotin, K. Sikes, Z. Jiang, M. Klima, G. Fudenberg, J. Hone, P. Kim, and H. Stormer, Solid State Communications **146**, 351 (2008).

[19] R. Peierls, Zeitschrift für Physik A Hadrons and Nuclei **80**, 763 (1933), 10.1007/BF01342591.

[20] M. O. Goerbig, Rev. Mod. Phys. **83**, 1193 (2011).

[21] C. R. Dean, A. F. Young, I. Meric, C. Lee, L. Wang, S. Sorgenfrei, K. Watanabe, T. Taniguchi, P. Kim, K. L. Shepard, and J. Hone, Nature Nanotechnology **5**, 722 (2010).

[22] N. Tombros, A. Veligura, J. Junesch, J. Jasper van den Berg, P. J. Zomer, M. Wojtaszek, I. J. Vera Marun, H. T. Jonkman, and B. J. van Wees, Journal of Applied Physics **109**, 093702 (2011).

[23] R. Maurand, P. Rickhaus, P. Makk, S. Hess, E. Tovari, C. Handschin, M. Weiss, and C. Schönenberger, "Fabrication of ballistic suspended graphene with local-gating," (2014), submitted.

[24] D. K. Cheng, *Field and Wave Electromagnetics*, 2nd ed. (Prentice Hall, 1989).

[25] A. Logg, K.-A. Mardal, G. N. Wells, *et al.*, *Automated Solution of Differential Equations by the Finite Element Method* (Springer, 2012).

[26] C. Geuzaine and J.-F. Remacle, International Journal for Numerical Methods in Engineering **79**, 1309 (2009).

[27] See supplemental material for numerical examples of the carrier density profile $n(x,y)$ simulated for the device, the carrier density as a function of energy and magnetic field $n(E,B_z)$ using scaled graphene ribbons, evaluation of the gate efficiency from the Landau fan diagram shown in Fig. 4(a), and comments on the speed-up and bilayer graphene.

[28] S. Datta, *Electronic Transport in Mesoscopic Systems* (Cambridge University Press, Cambridge, 1995).

[29] A. L. Grushina, D.-K. Ki, and A. F. Morpurgo, Appl. Phys. Lett. **102**, 223102 (2013).

[30] P. Rickhaus, R. Maurand, M.-H. Liu, M. Weiss, K. Richter, and C. Schönenberger, Nature Communications **4**, 2342 (2013).

[31] D. A. Abanin and L. S. Levitov, Science **317**, 641 (2007).

[32] J. R. Williams, L. DiCarlo, and C. M. Marcus, Science **317**, 638 (2007).

[33] B. Özyilmaz, P. Jarillo-Herrero, D. Efetov, D. A. Abanin, L. S. Levitov, and P. Kim, Phys. Rev. Lett. **99**, 166804 (2007).

[34] W. Long, Q.-f. Sun, and J. Wang, Phys. Rev. Lett. **101**, 166806 (2008).

[35] J. Tworzydło, C. W. Groth, and C. W. J. Beenakker, Phys. Rev. B **78**, 235438 (2008).

[36] M.-H. Liu, Phys. Rev. B **87**, 125427 (2013).

[37] G. Li and E. Y. Andrei, Nat. Phys. **3**, 623 (2007).

[38] E. McCann and M. Koshino, Reports on Progress in Physics **76**, 056503 (2013).

Supplemental Material

Carrier density profile of the simulated device

As mentioned in the main text, the finite-element simulator FEniCS [25] together with the mesh generator GMSH [26] are adopted to compute the self-partial capacitances [36] of the individual metal contacts and bottom gates, $C_{\mathrm{cL}}, C_{\mathrm{cR}}, C_{\mathrm{bogL}}$, and C_{bogR}, which are functions of two-dimensional coordinates (x,y). The classical contribution to the total carrier density $n(x,y)$ is given by the linear combination $\sum_{i=\mathrm{cL,cR,bogL,bogR}}(C_i/e)V_i$, where V_{bogL} and V_{bogR} are the left and right bottom gate voltages, respectively, and V_{cL} and V_{cR} are responsible for contact doping mainly arising from the charge transfer between the metal contacts and the graphene sheet. Since the experimental conditions are very similar to our previous work [30], we adopt the same empirical value of 0.04 V for both V_{cL} and V_{cR}. Total carrier density follows Ref. 36. Two examples showing $n(x,y)$ profiles are given in Fig. S1, where zero intrinsic doping is assumed.

Carrier-energy relation in the presence of magnetic field

To compute the carrier density as a function of energy E and magnetic field B_z using the Green's function method, we consider an ideal graphene ribbon extending infinitely along the $\pm x$ axis. The retarded Green's function tells the total density

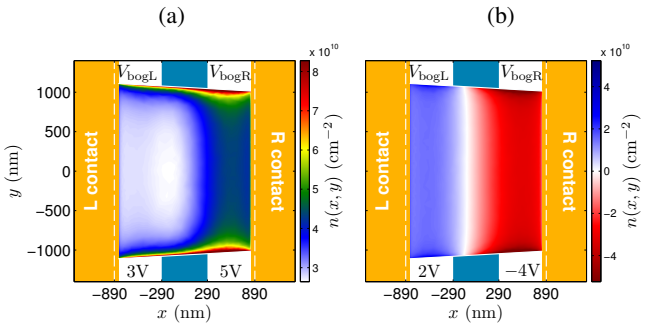

FIG. S1. Examples of carrier density profiles $n(x,y)$ with (a) unipolar and (b) bipolar gate voltage configurations. Bottom gate voltages are indicated in respective plots. The geometry follows the design values of the experiment, and the shape of the graphene flake is estimated from an optical image of the real device. The width of the bottom gates is 600 nm, and the white dashed lines indicate the edges of the bottom gates underneath the contacts.

of states of the supercell, $D(E,B_z) = -(1/\pi)\,\mathrm{Im\,Tr}\,G^r(E,B_z)$, where we have explicitly denoted the dependence of the magnetic field B_z, which enters from the tight-binding Hamiltonian of the supercell. The carrier density in the zero temperature limit is given by integrating over the energy, $n(E,B_z) = (2/A)\int_0^E D(E',B_z)dE'$, where the factor 2 accounts for the spin degeneracy and $A = N(3\sqrt{3}a^2/4)$ is the area of the supercell with N the number of lattice sites within the supercell and $a = s_f a_0$ the lattice spacing.

An example for $n(E,B_z)$ using a scaled armchair graphene ribbon with $s_f = 4$ and $N_a = 101$ (about 100 nm wide) is given in Fig. S2(a). With the increasing B_z, the emergence of the relativistic Landau level spectrum [37] is clearly seen, which

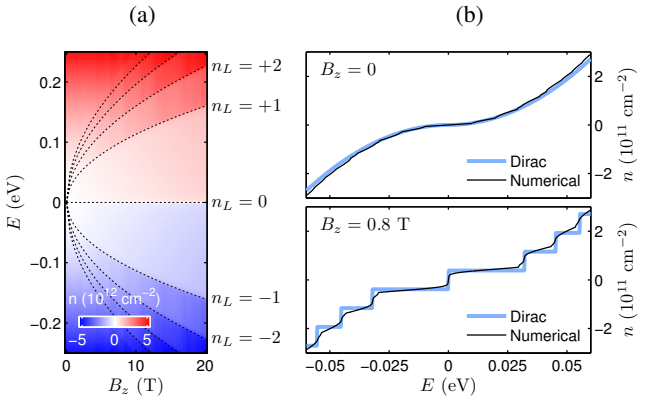

FIG. S2. (a) Carrier density as a function of energy E and magnetic field B_z, using an $s_f = 4, N_a = 101$ artificial armchair graphene ribbon (about 100 nm wide). The quantized carrier density is well described by the Landau level spectrum (dashed lines) given by Eq. (S1). (b) Carrier-energy relation at $B_z = 0$ (upper panel) and $B_z = 0.8$ T (lower panel), using an $s_f = 16, N_a = 50$ ribbon (about 200 nm wide). The numerical results are compared with the Dirac model, Eq. (S2) in the upper panel and Eq. (S3) in the lower panel.

is well described by

$$E_{n_L} = \mathrm{sgn}(n_L)E_1\sqrt{|n_L|} \quad , \quad n_L = 0, \pm1, \pm2, \cdots . \qquad \text{(S1)}$$
$$E_1 = \sqrt{2eB_z\hbar v_F^2}$$

Thus properly scaled graphene also correctly captures the half integer quantum Hall physics of real graphene.

In Fig. S2(b) we use another ribbon with $s_f = 16$ and $N_a = 50$ (about 200 nm wide) to compare the carrier-energy relation with and without magnetic field. For the $B_z = 0$ case [upper panel in Fig. S2(b)], despite the ribbon nature of the considered artificial graphene, the $n(E)$ relation is basically consistent with the Dirac model,

$$n_{\rm Dirac}(E) = \mathrm{sgn}(E)\frac{1}{\pi}\left(\frac{E}{\hbar v_F}\right)^2 . \qquad \text{(S2)}$$

For the $B_z = 0.8$ T case [lower panel in Fig. S2(b)], the numerical result exhibits quantized plateaus due to the Landau levels. The plateaus are, however, not perfectly flat due to the level broadening of the density of states, which stems from the finite width of the considered ribbon, instead of temperature.

In the case of ideal infinite graphene, the density of states can be written as $D_{\rm Dirac}(E,B_z) = (4eB_z/h)\sum_{n_L}\delta(E - E_{n_L})$, where the prefactor accounts for the states each Landau level can accommodate and E_{n_L} is given in Eq. (S1). Integrating $D_{\rm Dirac}(E,B_z)$ with respect to energy, one obtains a perfectly quantized carrier-energy relation

$$n_{\rm Dirac}(E,B_z) = \frac{4eB_z}{h}\left(\mathrm{sgn}(E)\left\lfloor\frac{E^2}{E_1^2}\right\rfloor + \frac{1}{2}\right), \qquad \text{(S3)}$$

where $\lfloor x \rfloor$ stands for the largest integer not greater than x (known as the floor function in computer science) and E_1 is given in Eq. (S1). Compared to the numerical $n(E,B_z)$ [lower panel in Fig. S2(b)], the ideal $n_{\rm Dirac}(E,B_z)$ given by Eq. (S3) is not suitable for describing the carrier-energy relation in finite-width graphene systems. Nevertheless, the formula confirms the correct trend of the numerical carrier-energy relation in the presence of magnetic field.

From the numerical $n(E)$ curve at a given B_z, such as that given in Fig. S2(b), the position of the highest filled energy level for a given carrier density, $E(n)$, is obtained, and the negative of it is the desired energy band offset for transport calculation as mentioned in the main text.

Gate efficiency from the Landau fan diagram

The pronounced quantized conductance plateaus reported in Fig. 4(a) of the main text allows for a precise evaluation of the gate efficiency. Let the average gate capacitance of the connected bottom gates be $\bar{C}_g$ and assume a uniform chemical doping of concentration n_0. Relating the mean carrier density given by $\bar{n} = n_0 + \bar{C}_g V_{\rm bog}$ and filling factor $\nu = \bar{n}/(eB_z/h)$ one finds

$$V_{\rm bog} = \frac{e\nu}{\bar{C}_g h}B_z - \frac{n_0}{\bar{C}_g} \equiv c_1\nu B_z + c_2 .$$

Thus on the field-gate map reported in Fig. 4(a) of the main text, the slope of each fan line that separates two adjacent conductance plateaus $\nu-2$ and $\nu+2$ gives $c_1\nu = e\nu/\bar{C}_g h$ while the intersect at $B_z = 0$ gives $c_2 = -n_0/\bar{C}_g$. By fitting the experimental data at $\nu = 0, \pm 4, \cdots$, we find $c_1 = 1.95\,\mathrm{V\,T^{-1}}$ and $c_2 = 0.3\,\mathrm{V}$, which yield a gate efficiency

$$\bar{C}_g = \frac{e}{c_1 h} = 1.24\times 10^{10}\,\mathrm{cm^{-2}\,V^{-1}}$$

and a weak chemical doping

$$n_0 = -c_2\bar{C}_g = -3.72\times 10^{9}\,\mathrm{cm^{-2}},$$

respectively. The deduced $\bar{C}_g$ is found to be slightly larger than the simulation [inset of Fig. 3(a) of the main text].

Comments on speed-up and bilayer graphene

The strongly reduced memory demand due to the scaling naturally lowers the computation time. Even for computable systems, the speed-up can be seen in, e.g., the computation time Δt for the lead self-energy that typically grows with the cube of the number of lattice sites within the lead supercell, i.e., $\Delta t \to \Delta t/s_f^3$ after scaling. Taking the illustrated 2.2-micron-wide graphene for example, Δt is found to be $\sim 2.4\,\mathrm{s}$ on a single Intel Core i7 CPU for the artificial graphene scaled by $s_f = 100$. For $s_f = 1$, the time required to compute just a single shot of the self-energy, if the memory allows, would be $\sim 2.4\times(100)^3\,\mathrm{s}$, which is almost a month.

The scaling can easily be shown to be applicable to bilayer graphene, whose low-energy spectrum is given by [38]

$$E(k) = \pm\sqrt{\frac{\gamma_1^2}{2}+\frac{U^2}{4}+\hbar^2 v_F^2 k^2 \pm \sqrt{\frac{\gamma_1^4}{4}+\hbar^2 v_F^2 k^2\left(\gamma_1^2+U^2\right)}}, \tag{S4}$$

with $\gamma_1 \approx 0.39\,\mathrm{eV}$ the interlayer nearest neighbor hopping and U the asymmetry parameter responsible for the gap. The appearance of the product ta in the dispersion (S4) after substituting $\hbar v_F = 3ta/2$ clearly suggests that the scaling condition [Eq. (1) of the main text] also applies for bilayer graphene with γ_1 and U left unaltered. Similar to the long wavelength limit [Eq. (2) of the main text] but due to the massive Dirac nature, the limit of s_f becomes stricter. In the case of gapless bilayer graphene, we have $s_f \ll 6\pi t_0/[(2|E_{\max}|+\gamma_1)^2-\gamma_1^2]^{1/2}$, which suggests $s_f \ll 50$ for the single-band transport ($|E_{\max}| \le \gamma_1$). In the presence of magnetic field, the restriction of Eq. (3) in the main text still applies.